MINIREVIEW

Check for updates

Photo-enhanced dehydrogenation of formic acid on Pd-based hybrid plasmonic nanostructures

Jiannan Zhu,[a] Jiawei Dai,[a] You Xu,[a] Xiaoling Liu,[a] Zhengyun Wang,[a] Hongfang Liu [ID][a] and Guangfang Li [ID] *[ab]

Coupling visible light with Pd-based hybrid plasmonic nanostructures has effectively enhanced formic acid (FA) dehydrogenation at room temperature. Unlike conventional heating to achieve higher product yield, the plasmonic effect supplies a unique surface environment through the local electromagnetic field and hot charge carriers, avoiding unfavorable energy consumption and attenuated selectivity. In this minireview, we summarized the latest advances in plasmon-enhanced FA dehydrogenation, including geometry/size-dependent dehydrogenation activities, and further catalytic enhancement by coupling local surface plasmon resonance (LSPR) with Fermi level engineering or alloying effect. Furthermore, some representative cases were taken to interpret the mechanisms of hot charge carriers and the local electromagnetic field on molecular adsorption/activation. Finally, a summary of current limitations and future directions was outlined from the perspectives of mechanism and materials design for the field of plasmon-enhanced FA decomposition.

Introduction

The global environmental problems and energy crises caused by the exhaustion of fossil fuels have forced us to search for feasible alternatives. As green and efficient energy, hydrogen (H_2) is the most promising alternative to traditional fossil fuels because of its high calorific value and non-toxic emission.[1–3] However, the storage and transportation of hydrogen is the biggest challenge for large-scale hydrogen energy utilisation. Organic liquid hydrogen carriers provide an effective guide for hydrogen storage and transportation. Formic acid (FA, HCOOH) is considered as a promising hydrogen carrier owing to its nontoxicity, wide availability from biomass raw materials, and considerable hydrogen capacity (4.4 wt%).[4–8] H_2 release from FA is thermodynamically feasible, while the kinetics is extremely slow. Pd is viewed as the most efficient heterogeneous catalyst for FA dehydrogenation (HCOOH → H_2 + CO_2).[7,9,10] However, its catalytic performance is still not satisfying.

During the past decades, much effort has been devoted to utilizing light energy to boost the catalytic dehydrogenation of Pd catalysts.[11–15] In particular, when coupled with plasmonic noble metals such as Au or Ag, the Pd-based plasmonic hybrid mechanism demonstrated a greatly improved catalytic selectivity, activity, and toxicity resistance for catalytic FA

decomposition under light illumination in a mild environment.[11,14,16] This hybrid plasmonic system simultaneously acts as a light absorber and a catalytically active site. Such an enhancement mechanism originates from the plasmonic effect.

Upon illumination, plasmonic nanoparticles (*i.e.*, Au, Ag, Cu, Al) support localized surface plasmon resonance (LSPR)-collective oscillations of electrons at the surface when the natural frequency of the electron coincides with the incident wavelength.[20–32] A key LSPR feature is the large extinction associated with the surface
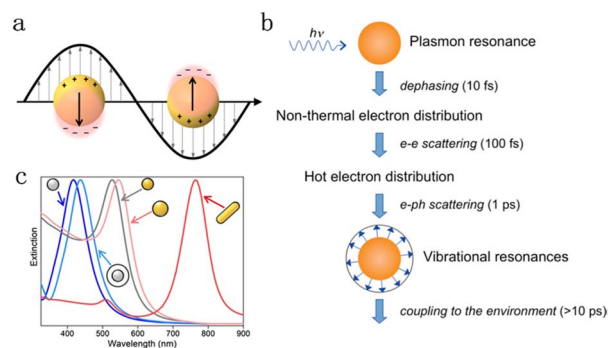

Fig. 1 (a) Surface enhanced electromagnetic field caused by collective electron oscillations.[17] Reproduced with permission from ref. Copyright 2018 American Chemical Society. (b) Decay sequence and approximate time scale of metal nanoparticles after light excitation.[18] Reproduced with permission from ref. Copyright 2011 American Chemical Society. (c) Extinction spectra of Ag (gray) and Au (yellow) nanoparticles with different sizes, shapes, and dielectric environments (with/without a white silica shell).[19] Reproduced with permission from ref. Copyright 2023 Wiley-VCH.

[a]*Key Laboratory of Material Chemistry for Energy Conversion and Storage (Ministry of Education), Hubei Key Laboratory of Material Chemistry and Service Failure, School of Chemistry and Chemical Engineering, Huazhong University of Science and Technology, Wuhan 430074, PR China. E-mail: guangfl@hust.edu.cn*

[b]*Shenzhen Huazhong University of Science and Technology Research Institute, Shenzhen, 518000, PR China*

Table 1 The FA dehydrogenation rate of over various Pd-based heterogeneous catalysts

No.	Catalysts	H$_2$ evolution rate [mmol g^{-1} h^{-1}]		Light intensity [mW cm^{-2}]	Temperature [°C]	Reference
		Dark	Light			
1	Pd-covered Au NRs	0.4	5.3	100	5	16
2		1.8	6.7		25	
3		7.5	22		40	
4	Pd-tipped Au NRs	0.6	8.7		5	
5		2.7	10.5		25	
6		10	32.5		40	
7	Pd-covered Ag@Au HNPs	~0	3	500	15	14
8		3	7.5		25	
9		12	15		50	
10	Pd-dotted Ag@Au HNPs	2	29		15	
11		10	35		25	
12		25	105		50	
13	Au@Pd shell	0.5	1	125	40	38
14	Au@AuPd shell	1	5			
15	Au–Pd satellites	35	90			
16	Au–AuPd core–satellites	70	191			
17	Au$_1$Pd$_3$/GO	8.2	16.4	100	25	13
18	Au$_1$Pd$_2$/GO	11.7	22.2			
19	Au$_1$Pd$_1$/GO	7	16.6			
20	Au$_2$Pd$_1$/GO	3.7	9.4			
21	Au$_3$Pd$_1$/GO	1.2	3.5			
22	Pd/GO	0.9	1.6			
23	Au@Pd/UiO-66(Zr$_{85}$Ti$_{15}$)	1517	1875	320	30	39
24	PdAg@g-C$_3$N$_4$	6.1	9.8	—	25	40
25		—	27.6		50	
26	AgPd/CN-3%	2.1	5.9	—	30	41
27	NiAuPd	29	69	121	5	12
28		183	341		25	
29		441	641		45	
30	Au1@Pd	15.9	58.5	121	25	11
31	Au2@Pd	14.6	42.1			
32	Au3@Pd	8.4	14.7			
33	Au4@Pd	5.3	12.9			

oscillating electromagnetic field (Fig. 1a),[17] which is closely related to the size, composition and geometry of plasmonic particles.[21,25,33–37] As shown in Fig. 1b, a decay of electron collective oscillations generates radiative scattering of photons or non-thermal energetic carriers (hot electrons and hot holes) at the femtosecond scale, which then redistributed to form thermal hot carriers through electron–electron scattering.[18] Finally, the electron–hole pair relaxation occurs *via* electron–phonon and phonon–phonon scattering, and the energy dissipates into the environment over a longer time horizon, resulting in localized heating effects. For pure Au and Ag nanoparticles, their extinction ranges concentrate in the visible region and are widely used as platforms for light absorption (Fig. 1c).[19] The FA dehydrogenation rate can be significantly enhanced through the LSPR-induced electromagnetic field and hot charge carriers by rationally combining a plasmonic metal with Pd. Examples of plasmon-enhanced FA dehydrogenation are summarized in Table 1. Nevertheless, the mechanism of LSPR effect on FA dehydrogenation is still undefined. It is significant to reveal the fundamentals of the electromagnetic field and hot charge carriers on molecular adsorption/activation to deepen the understanding of this growing research field.

In this review, we introduce the recent progress in plasmon-enhanced FA dehydrogenation, summarize the influence of the size/geometry on plasmon catalysis, and discuss the impact of electronic structure from the perspective of Fermi-level engineering and alloying. Then, we summarize the mechanisms of hot charge carriers and local field work in FA dehydrogenation. Some representative cases are covered to discuss the plasmonic energy dispersion in space and the unique advantages of LSPR in reactant adsorption/activation, which may inspire exploring and understanding the plasmon-enhanced FA dehydrogenation. Finally, we present an outlook and propose some suggestions applicable, but not limited to, obtaining higher FA dehydrogenation activity *via* hybrid plasmonic metal nanostructures.

Plasmon-enhanced activity

Au and Ag are the most popular plasmonic metals for plasmonic catalysis, and their LSPR properties are heavily dependent upon their morphology, size and composition.[42–45] For plasmon-enhanced FA dehydrogenation, the core–shell heterostructure is the most commonly reported nanostructure, and the typical

fabrication is the reduction of a Pd-containing salt precursor on previously synthesized colloid plasmonic seeds, *i.e.*, the seed-mediated method.[46–50] Generally, pre-synthesized plasmonic nanoparticles of different shapes/sizes are selected as cores, which can coarsely determine the overall LSPR properties. Then, by adjusting the relevant thermodynamic and kinetic factors, the growth mode of the shell metal can be precisely controlled. Therefore, geometric control engineering can be well achieved in terms of the core and shell in principle. This section focuses on the effects of geometry-determined optical properties on FA decomposition performance.

Size effect

The extinction spectra of Au nanostructures show a strong dependence on their size when exceeding the quasi-static limit.[51–53] For spherical Au nanoparticles with a size larger than 5 nm, strong plasmon resonances occur in the visible region (about 520–600 nm). When the diameter is less than 5 nm, the LSPR is dramatically suppressed, which significantly blue shifts and eventually disappears once the particle size < 2 nm. The particle size dramatically affects the optical properties of plasmonic nanostructures, such as absorption and scattering efficiencies, and the intensity of near-field enhancements, all of which make great contributions to catalytic performance in plasmonic catalysis. A spherical metal with a diameter smaller than the incident wavelength can be approximated as a dipole. The following formula (1) can express the corresponding particle polarizability α under excitation,[54–56]

$$\alpha = 4\pi\varepsilon_m r^3 \frac{\varepsilon - \varepsilon_m}{\varepsilon + 2\varepsilon_m} \quad (1)$$

where ε_m is the dielectric constant of the surrounding medium (non-absorbing), r is the particle radius, and ε is the wavelength-dependent complex dielectric function, including the real part (Re) and imaginary part (Im). And it can be found that the polarizability increases with the increase in diameter. Further derivations can be made to obtain far field extinction, absorption, and scattering cross-sections (2)–(4),[54]

$$\sigma_{abs} = \frac{24\pi^2\varepsilon_m^{\frac{3}{2}} r^3}{\lambda} \frac{Im[\varepsilon]}{|\varepsilon + 2\varepsilon_m|^2} \quad (2)$$

$$\sigma_{sca} = \frac{32\pi^4\varepsilon_m^2 r^6}{\lambda^4} \frac{|\varepsilon - \varepsilon_m|^2}{|\varepsilon + 2\varepsilon_m|^2} \quad (3)$$

$$\sigma_{ext} = \sigma_{abs} + \sigma_{sca} \quad (4)$$

It can be found that the absorption is proportional to r^3, while the scattering is proportional to r^6. When r is much smaller than the incident wavelength, extinction is essentially dominated by absorption. The scattering ratio in extinction increases significantly with the increase of the size.

The influence of the size effect may be different in different reaction systems, since different rate-determining steps are involved, and the size-dependent near and far field properties

may not contribute constantly in different plasmon-enhanced processes. For example, Christopher *et al.* studied the plasmon-enhanced O_2 dissociation on Ag nanostructures with various sizes and found that the quantum efficiency was consistent with the near-field enhancement rather than the hot carrier density in different photon wavelength tests (Fig. 2a), which clearly proved that O_2 dissociation was related to the strong LSPR local electromagnetic field.[57] However, as reported by Li and co-workers in 2017, Ag nanoparticles with intermediate sizes (25 and 50 nm), which balanced the light absorption and local electromagnetic field, exhibited the best photocatalytic rates (Fig. 2b).[58] In our previous work, we synthesized different-sized Au@Pd nanospheres with narrow size distributions to clarify the role of size effect in FA dehydrogenation over Pd-based hybrid plasmonic catalysts.[11] The Au core size varied from 56 to 121 nm to ensure visible light range absorption, while the thickness of the shell comprising Pd nanodots was kept consistent. The optical properties of Au@Pd core–satellite nanospheres were dominated by the Au core, including the LSPR position, absorption, and scattering. With the increase of the Au diameter, the absorption ratio of the hybrid plasmonic catalyst decreases, while the far-field scattering and near-field intensity increase instead. The smallest Au@Pd nanospheres, exhibiting the highest absorption/extinction ratio, demonstrated the best catalytic performance (Fig. 2c and d). Interestingly, large, relatively high scattering nanospheres demonstrated a higher-than-expected catalytic enhancement factor, approaching the same value as the smallest ones (Fig. 2e) by moderately raising the reaction temperature or shortening the interparticle distance by increasing the catalyst concentration, which was ascribed to the reduced interparticle spacing
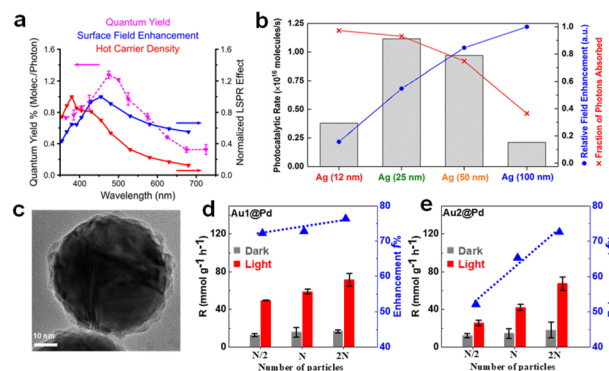

Fig. 2 (a) Correlation between the wavelength dependent O_2 dissociation quantum yield and LSPR effects including field enhancement and carrier density.[57] Reproduced with permission from ref. Copyright 2019 American Chemical Society. (b) The photocatalytic rates, field enhancements, and fractions of photons absorbed in the catalyst bed for four Ag@SiO$_2$/Pt heterostructures with different Ag NP sizes.[58] Reproduced with permission from ref. Copyright 2017 American Chemical Society. (c) TEM image of an individual Au1@Pd NP. The correlation of H$_2$ evolution rate and enhancement *f* with the particle concentration, (d) Au1@Pd and (e) Au2@Pd samples, respectively. N represents the original particle numbers.[11] Reproduced with permission from ref. Copyright 2022 American Chemical Society.

that promotes the secondary absorption of scattered photons (multiple scattering effects) and drastic near-field enhancement between the neighbouring particle region.[59–62] Therefore, in the case of FA dehydrogenation on Pd-based hybrid plasmon metal, both hot charge carriers and the near-field were involved in accelerating dehydrogenation.

Morphology effect

Unlike Au nanospheres, Au nanorods (NRs) exhibit more special plasmon resonances due to their anisotropic structure.[37,46,63,64] The electron oscillates along the short axis and resonates with the light in the 510–530 nm wavelength range, named transverse surface plasmon resonance absorption (TSPR); meanwhile, another vital LSPR along the long axis is attributed to the longitudinal LSPR, which typically distributes in the visible to near-infrared region. Considering its strong oscillation, the longitudinal LSPR exhibits a more significant impact on optical properties and sequential catalytic activity. For example, Zheng synthesized two kinds of anisotropic Au–Pd nanorods, Pd-covered Au NRs with a thin Pd layer completely covering the Au NRs (Fig. 3a) and Pd-tipped Au NRs with Pd nanocrystals selectively deposited at the Au NR tips (Fig. 3b).[16] Such structural difference results in different photochemical conversion efficiencies; Pd-tipped Au-NRs exhibit better plasmon-enhanced activity for FA dehydrogenation, while a comparable light-driven enhancement factor was observed for both samples. Single-particle photoluminescence (PL) spectroscopy was applied to reveal the plasmon-induced pathway, especially the interfacial interaction between Au and Pd. The results in Fig. 3c and d show that the quenching efficiency of longitudinal LSPR reached 87–95%, while TSPR exhibited a similar intensity with pure Au NRs for both samples. According to the accepted PL mechanism, the quenching results from the effective charge separation, which avoids the recombination of the hot charge carriers; the luminescence mainly originates from the LSPR radiative decay of Au NRs, and PL damping indicates that the

radiation tunnelling becomes suppressed and more plasmon energy disperses through the electron transfer from Au to Pd. The finite-difference time-domain (FDTD) method was also carried out to investigate the effect of the plasmon resonance energy transfer (PRET) process to further confirm the interaction of Pd with the Au NR, which showed that the enhancement of electric field intensity around the tips was much stronger than that around the sides, revealing that the plasmon energy can be effectively utilized by locating the active metal at the sites with the intense field.

Such a selective deposition of active species at the field-enhanced sites has also been applied in other plasmonic hybrid catalysts. For instance, Xiao *et al.* prepared Pt end-deposited bimetallic nanostructures (ePt-Au NBPs) over Au nano-bipyramids (Au NBPs), which have a similar LSPR property to Au NRs.[65] Compared to the all-deposited aPt-Au NBPs, the maintained strong field at the sharp tips can promote the generation and migration of the carriers and then boost the spontaneous reconstruction of the Pt surface to produce more active sites.

This design strategy has also been validated in theoretical studies. Linic *et al.* studied the absorption/scattering of Au@Pt NRs through the finite element method (FEM).[66] The absorption intensity of longitudinal LSPR becomes much higher than that of pure Au NRs, while no significant changes appear in the TSPR region, which is attributed to the ratio of the dielectric function imaginary part for Pt to Au being much higher at low energy than in high plasmon mode, resulting in the plasmon energy being preferentially dissipated in the Pt shell at the longitudinal LSPR position rather than TSPR.

By switching nanorods to nanoplates, Huang *et al.* reported that Pd-dotted Ag@Au nanoplates exhibited an improved catalytic activity normalized to Pd mass under identical reaction conditions.[14] They selectively deposited Pd nanodots on the surface of Ag@Au nanoplates and obtained a two-shell geometry (Fig. 3e), including continuous Pd coverage (Pd-covered Ag@Au) and discrete Pd decoration (Pd-dotted Ag@Au), in which Pd-dotted Ag@Au manifested a higher FA dehydrogenation rate and plasmon enhancement factor. As shown in Fig. 3f, single-particle PL intensity experiments revealed significant quenching in Pd-dotted Ag@Au compared to Ag@Au, verifying a transfer of hot electrons from Ag@Au to Pd dots and leading to surface charge heterogeneity. Such structure–activity difference results from the combined effect of the optical absorption and the local field. Compared to a fully covered Pd shell, discrete Pd dots do not completely block the absorption of photons by Ag@Au. The FDTD further confirmed that the uplifted Pd dots exhibit a steep gradient field. However, unlike the selective deposition mentioned above, such Pd dots did not intentionally couple with the field sites but affected the electromagnetic spatial distribution through their non-plasmonic geometry and thus enhanced chemisorption and bond activation.

Fig. 3 The TEM images of (a) Pd-tipped Au NRs and (b) Pd-covered Au NRs. (c) The relationship between PL intensities and diameter in different plasmon modes of single Au NRs and Pd-tipped Au NRs. (d) The PL quenching efficiency of single Pd-tipped (red dots) and Pd-covered (blue dots) Au NRs with different diameters.[16] Reproduced with permission from ref. Copyright 2015 American Chemical Society. (e) The TEM image of Pd-dotted Ag@Au. (f) The PL intensity of individual Ag@Au and Pd-dotted Ag@Au.[14] Reproduced with permission from ref. Copyright 2020 Elsevier.

Coupling LSPR with Fermi level engineering

In conventional thermal FA dehydrogenation, a mature strategy is to promote surface charge heterogeneity (increase the electron density on the Pd surface) to obtain a higher
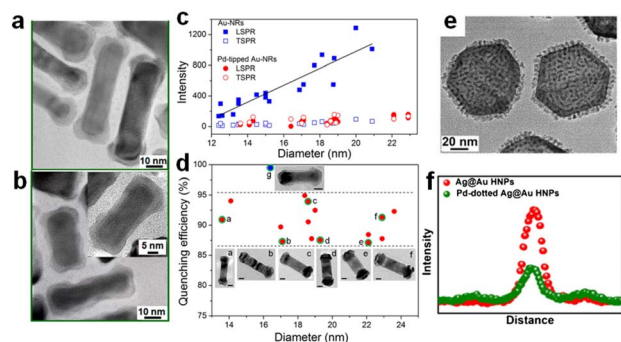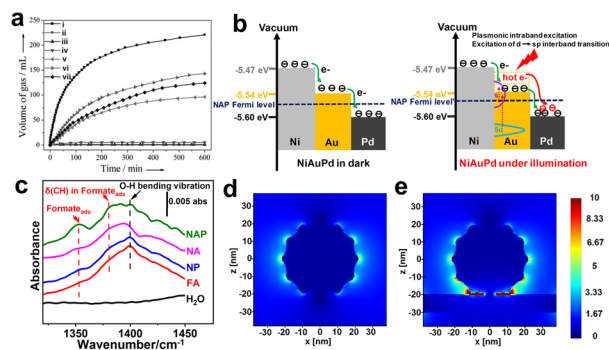
Fig. 4 (a) Real-time gas volume production diagram in the presence of (i) $Co_{0.30}Au_{0.35}Pd_{0.35}$/C, (ii) Co/C, (iii) Au/C, (iv) $Co_{0.30}Au_{0.70}$/C, (v) Pd/C, (vi) $Co_{0.30}Pd_{0.70}$/C, and (vii) $Au_{0.50}Pd_{0.50}$/C at room temperature.[69] Reproduced with permission from ref. Copyright 2013 Wiley-VCH. (b) Schematic diagram illustrates the charge transfer within NiAuPd under darkness (left) or under radiation (right). (c) ATR-FTIR spectra of HCOOH and formate-related intermediate co-adsorption over various catalysts. The distribution of the electromagnetic field of (d) AuPd, and (e) trimetallic NiAuPd in space.[12] Reproduced with permission from ref. Copyright 2022 Wiley-VCH.

dehydrogenation rate.[67,68] For example, Tsang and co-workers prepared a series of core–shell nanostructures in which the shell is a thin Pd layer, while the cores are composed of various metals (M) with different work functions.[7] A simple linear relationship between the HCOOH decompose rates, and the work function of M fcc (111) can be obtained, indicating that the electron redistribution forced by Fermi level equilibrium plays a vital role in promoting FA dehydrogenation. Moreover, as shown in Fig. 4a, Jiang et al. utilized the difference in work functions between Co, Au, and Pd to prepare an efficient CoAuPd/C catalyst, which effectively regulated the electron density of Pd sites and exhibited the best FA dehydrogenation activity at room temperature.[69]

Inspired by this, we reported a trimetallic NiAuPd heterogeneous catalyst, which synergistically combines Fermi level engineering and plasmon effect of promoting the surface charge heterogeneity, resulting in an enhanced intermediate chemisorption and ultimately promoted plasmonic catalysis (Fig. 4b).[12] Under darkness, electrons transfer from Ni (high Fermi level) to Au and Pd due to the work function differences, and Au acts as an electron-mediated channel to promote charge migration. Such intrinsic electronic structure enables NiAuPd to exhibit a significant O–H cleavage and formate-related intermediate chemisorption (Fig. 4c). Under irradiation, compared with the AuPd or NiO–AuPd, a higher Fermi level in NiAuPd allows hot electrons to upshift into a more energetic state after absorbing a photon. Furthermore, the FDTD in Fig. 4d and e demonstrates that the narrow gaps between Au–Pd and Ni plate create a fierce field; such hot spots can boost C–H activation through a direct energy flow.

Combination of alloying and support

Different from the core/shell heterostructure discussed above, Pd-based alloys have also been well studied in FA

dehydrogenation due to the alloying effect, which can delicately modify the electronic structure of the catalytically active metal via d-orbital overlap or metal surface segregation.[70–74] Various alloyed nanocatalysts have demonstrated improved catalytic behaviors via strain/ligand effect and/or ensemble effect in traditional thermal catalysis.[75–78] During the past decades, Pd-based plasmon alloys have also been explored to combine plasmonic enhancement with intrinsic alloy effect, while most reports involve semiconductor supports, because the photon/plasmon response can lead to dramatic changes in the electronic structure and thus the overall reactivity of the complex catalyst through the electronic interaction between the plasmonic metal and semiconductor resulting from the Mott–Schottky effect. It has been well demonstrated that the charge kinetics of photocatalytic reactions could be able to accelerate photocatalytic FA decomposition by integration of plasmonic-based alloys (AgPd and AuPd) and semiconductors to make Mott–Schottky photocatalysts. Carbon nitride (g-C_3N_4), one of the most important semiconductors,[79–81] has been widely used as a semiconductor support in hydrogen generation due to its efficient handover of photogenerated electrons to plasmonic hybrid nanoparticles. For example, a monodisperse alloy of AgPd on a graphite carbon nitride semiconductor (AgPd/CN) was used for photocatalytic evolution of hydrogen from formic acid.[41,82] Stucky et al. prepared the AgPd alloy shown in Fig. 5a–d on the surface of CN.[41] The electron transfer from CN and AgPd leads to an electron-enrichment of Pd and thus affords more catalytic activity and stability for the H_2 evolution under visible light. In another example, small (3 nm) AuPd nanoparticles were loaded on carbon nitride nanospheres (AuPd/CNS) for the design of Mott–Schottky catalysts, Liu et al. found that Mott–Schottky, alloying and plasmonic effects can be used in conjunction with each other to efficiently accelerate the electron transfer from photoresponsive super small carbon nitride nanospheres to plasmonic alloys (Fig. 5e), which eventually
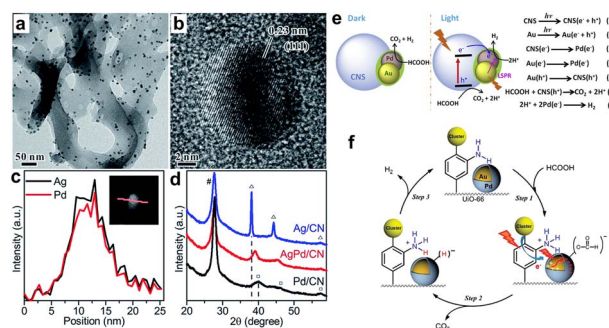

Fig. 5 The (a) TEM and (b) HR-TEM images of AgPd/CN. (c) The qualitative line scan of an individual AgPd nanoparticle over CN. (d) The XRD patterns of different samples prepared by the same method.[41] Reproduced with permission from ref. Copyright 2017 Royal Society of Chemistry. (e) The mechanism diagram of photocatalytic hydrogen evolution from formic acid for AuPd/CNS with/without irradiation.[15] Reproduced with permission from ref. Copyright 2019 Elsevier. (f) Possible mechanism for plasmon-enhanced H_2 production by Au@Pd/UiO-66.[39] Reproduced with permission from ref. Copyright 2017 American Chemical Society.

leads to a remarkable photocatalytic activity for the photo-catalytic hydrogen evolution from formic acid.[15]

In addition to building the Mott–Schottky effect, some other materials such as metal organic frameworks (MOFs),[39] carbon-based materials,[13,83] and wide-bandgap oxides (e.g., ZrO_2)[84,85] are often employed. For example, Yamashita et al. loaded Au@Pd nanoparticles on the surface of an amine-modified MOF (UiO-66($Zr_{100-x}Ti_x$)) for boosting FA dehydrogenation under light.[39] More importantly, the amine functionality in the MOF and the electron-rich state of Pd upon plasmon excitation synergistically promote FA decomposition. As shown in Fig. 5f, weakly alkaline –NH_2 acts as a proton scavenger to positively promote O–H dissociation and form –$^+HNH_2$. After photon absorption, the electron-rich state on the Pd surface helps the chemisorbed formate intermediates break C–H. Thus, the weakly basic synergistic combination of amine groups and LSPR effects accounts for its high catalytic activity.

Mechanism insight

Strong LSPRs enable plasmonic metals to convert incident photons to hot carriers, strong electromagnetic fields, or thermal heat for directing and improving chemical reactions. By combining plasmonically active metals with traditionally catalytic metals, plasmonic hybrid nanostructures could simultaneously promote light conversion and molecular solid adsorption. Some efforts have been devoted to the plasmon-induced contribution, while the mechanism is more complex. This section will discuss plasmon enhancement from the perspective of hot carriers and local electromagnetic fields.

Hot charge carriers

In plasmonic catalysis, a hot charge carrier is widely regarded as one of the main mechanisms in promoting bond activation.[20,86,87] For a simple hybrid system composed of a plasmonic metal and an adsorbed molecule, there are two recognized charge transfer pathways, indirect and direct charge transfer.[20,22,88,89] In an indirect path, hot carriers are generated within the metal through Landau damping, and then injected into neighbouring chemisorbed molecules before fundamentally thermalizing into a low-energy carrier or recombination. However, in a direct charge transfer, plasmonic nanoparticles and adsorbed molecules are not treated as two individual electronic states, but a new hybrid electronic state formed at the metal–molecule interface, which can participate in LSPR exci-tation, energy decay, and distribution, and this process is also known as chemical interface damping (CID).[90,91] More impor-tantly, this direct route is believed to be more efficient because it is momentum conserved without involving energy loss induced by electron–electron and electron–phonon scattering within metal body.

Experiments and theoretical simulations have also verified that direct charge transfer can take place in solid-state hybrid plasmonic systems. For example, Linic's group deposited a thin Pt layer (1 nm) on the surface of Ag nanocubes (75 nm edge length).[92] It is found that absorption is the main decay route for Ag–Pt, and the ratio of absorption is larger for a Pt shell (Ag–Pt) compared to the Ag shell (pure) for identical Ag nanocubes, while the radiative decay occupied a larger proportion in extinction for pure Ag nanocubes. That is, almost all the elec-tromagnetic field energy of Ag is dissipated through the Pt shell (forming $e^-–h^+$ pair), which is attributed to the fact that the imaginary part of Pt is larger than that of Ag in the visible range, and the plasmonic local field further enhances this absorption channel.

After summarizing the current views on the spatial disper-sion of LSPR energy in the metal–metal system, we still need to know the role of hot charge carriers in promoting FA dehydro-genation. Generally speaking, upon light irradiation, the adsorbed state could be excited by LSPR, and the hot carrier injection (or direct excitation within the molecule/interfacial metal-adsorbent) makes the complex reach a charged (or excited) state, thus obtaining nuclear kinetic energy and chemical bond activation. Specifically, Zheng et al. studied the PL spectra of the single particles of Au–Pd impregnated with FA solution (Fig. 6a), and the results showed that the PL intensity was significantly quenched, indicating that the hot electrons were injected into the FA molecule.[93] When the surface of Au–Pd was covered with Al_2O_3 to isolate the charge transfer channel, the PL quenching was not observed, which further confirms that the hot electron is an essential factor in enhancing FA dehydrogenation. In addition, density functional theory (DFT) calculations revealed that adding an electron on the surface of Pd atoms can effectively reduce the Gibbs free energy of the adsorbed state of FA molecules and intermediates (Fig. 6b), illustrating that optimizing the interfacial electronic properties can facilitate the dehydrogenation.[94] In addition to hot elec-trons, hot holes are also believed to promote FA dehydrogena-tion. As shown in Fig. 6c, Moskovits et al. proposed that hot
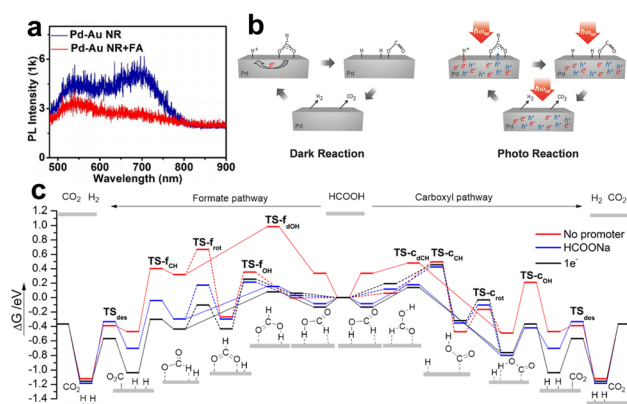

Fig. 6 (a) The PL intensities of individual Pd-tipped Au NRs and the signal after immersing in FA aqueous (1 M).[93] Reproduced with permission from ref. Copyright 2021 American Chemical Society. (b) Gibbs free energy reaction profiles (eV) for FA dehydrogenation over Pd (111) via the formate (left) and carboxyl (right) pathway. The slab surface is modified by various methods: no promoter, HCOONa ($HCOO^-$ and Na^+), and $1e^-$.[94] Reproduced with permission from ref. Copyright 2017 American Chemical Society. (c) Illustrations of the mechanism in plasmon accelerating FA decomposition.[95] Reproduced with permission from ref. Copyright 2016 Wiley-VCH.

electrons/holes boost the neutralization rate cooperatively to reduce the activation energy, in which holes are injected into negatively charged formates to accelerate C–H fracture, while hot electrons neutralize –H$^+$ to accelerate H_2 desorption.[95]

Local electromagnetic field

For surface-chemisorbed molecules, the local electromagnetic field can significantly modify their bond length, configuration, *etc*, which can flatten the potential energy surface (PES) and reduce the activation energy barrier, although the molecules cannot be excited to the excited state within the femtosecond scale lifetime range.[96] Beyond that, the selective effect of local electromagnetic fields on adsorption configurations has been discovered in recent years. Compared with nonpolar or weak-polar reactants, the plasmon force can more easily influence molecules with large dipole moments, thus changing the diffusion and adsorption behavior. For instance, Zhu and co-workers observed a photo-switching product selectivity in the alkyne–hydroamination reaction, where the product selectivity depends on the ratio of surface chemisorbed reactants.[84] Alkynes and anilines exhibit different chemisorption types with/without irradiation. In the dark, numerous alkynes are adsorbed on the surface sites and produce Diyne. Upon illumination, the alkynes are released from the surface, while the light-polarizable aniline is preferentially adsorbed and driven by plasmon forces to obtain Imine. Considering the large dipole moment of HCOOH and some additives (*e.g.*, HCOONa), such plasmon force can also optimize the interfacial adsorption configuration in FA dehydrogenation.

The local field-assisted FA activation was judged by the Au–Pd core–shell and core–satellite nanostructures. Emiliano and collaborators prepared the Au@Pd shell and Au@AuPd shell, and assembled the Au–Pd satellite and Au–AuPd satellite to study FA dehydrogenation under darkness and light.[38] The results in Fig. 7a and b show that the geometric structure can profoundly influence the dehydrogenation activity. Among these, the Au–AuPd satellite has the highest dehydrogenation rate and enhancement factor due to the gap between the reactor and the plasmon antenna, allowing the electromagnetic field to climb up to almost 30 times larger than the surface of the Au@Pd core–shell (Fig. 7c). Meanwhile, the higher dielectric function imaginary enables the e$^-$–h$^+$ to almost form in Pd after the plasmon decay (Fig. 7d).

Beyond FA dehydrogenation, hot spots located at interparticle gaps were extensively studied in the antenna–reactor geometry. In this typical system, no obvious interfacial hybrid state was created between the antenna and reactor, which are usually physically separated or isolated by insulators (such as SiO_2).[87,97–101] According to Sytwu's work, an antenna–reactor system where Au–Pd is physically mixed, the β phase Pd nanocubes exhibit a faster transition rate to the α phase under illumination.[102,103] And the Pd closer to the plasmon antenna always transitions faster than those far away from the antenna. Hot spots contribute to the nucleation at Pd nanocube edges rather than the corners (low-coordination sites), implying that the electromagnetic field assists in creating new sites, even though these sites are energetically unfavorable.
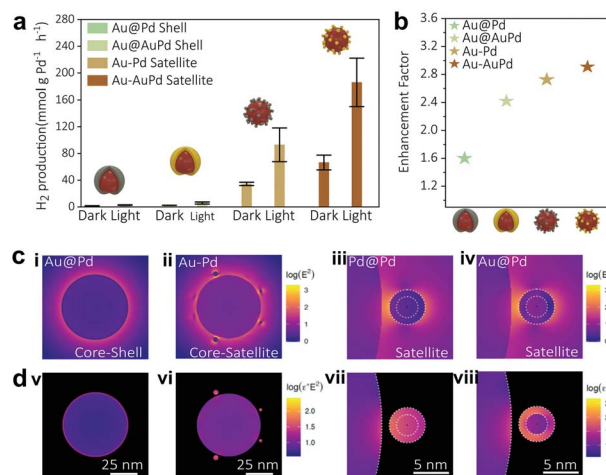

Fig. 7 (a) The H_2 production of various bimetallic nanocatalysts under dark conditions and upon illumination, and (b) their corresponding enhancement factors (the ratio between light and dark performances). (c) Electric field distribution for various bimetallic nanocatalysts, (i) Au@Pd core–shell, (ii) Au–Pd core–satellite, (iii) a Pd satellite and (iv) Au@Pd satellite placed 1 nm away from an antenna, and (d) corresponding absorption maps of (v) Au@Pd core–shell, (vi) Au–Pd core–satellite, (vii) a Pd satellite and (viii) Au@Pd satellite.[38] Open Access ref. from 2022 Wiley-VCH.

As a powerful tool, DFT calculation can well investigate the influence of electromagnetic fields on reaction thermodynamics, intermediates, hybrid electronic states, and so on.[86,104–106] The hybridized orbitals at the interface are redistributed under the action of electromagnetic fields, which may contribute to the direct dissipation of plasmon energy in these metal-molecular states. Such momentum conservation excitation avoids the metallic electron–electron and electron–phonon relaxation, resulting in some selective activation scenarios, and some unexpected phenomena. In a recent study, the projected density of states (PDOS) was used to analyze interfacial hybridization states when CuPd was employed as an adsorption site for CO_2.[105] When an electric field was introduced to simulate the LSPR collective electron oscillation, the hybridized O1 2P and O2 2P shifted away from the Fermi level and became more overlapped, further stabilizing the interfacial adsorption configuration. More impressive, new quasi-isolated states are generated near the Fermi level, contributing to the oscillation of more electronic states and the extension of hot carrier lifetimes.

Perspective and outlook

Although great progress has been made during the past decades in the field of light-enhancing FA dehydrogenation, to move forward, further improvement complemented by both theoretical and experimental advances is essential to establish a more quantitative understanding of hybrid plasmonic metal nanostructures. This section focuses on major limitations and further development for plasmon-enhanced FA dehydrogenation.

(1) Mechanism investigation. Compared with thermal catalysis, the physicochemical understanding of plasmon-involved chemical reactions is still far from clear, such as

plasmon-induced configuration transformation and specific contributions of hot carriers and electromagnetic fields. In addition, some additives (*e.g.*, HCOONa) are widely employed to boost H_2 evolution in traditional thermal catalysis, while the role of additives in plasmonic catalysis still needs to be determined. Advanced characterization and theoretical simulations provide promising approaches to explore the underlying mechanism in plasmon-enhanced FA dehydrogenation. Advanced techniques with fine temporal, spatial, and energy resolution, such as tip-enhanced Raman scattering (TERS),[107–110] surface-enhanced Raman scattering (SERS),[111–113] and synchrotron infrared nanospectroscopy (SINS),[114,115] *etc.*, can be used to obtain molecular vibrations, intermediate conversion, and energy dissipation at a picosecond level or in a specific nanoscale region, which is helpful to determine multiple effects. Theoretical simulation provides another convenience for obtaining high-quality information, including chemisorbed structure, hybrid electronic density of states, intermediates, and so on, which can deepen the understanding of plasmon energy conversion and guide the rational design of catalyst systems.[86]

(2) Plasmonic catalyst design principles. The ability of light absorption is essential for plasmonic catalysis. Within the mean free path, the optical absorption is positively correlated with the square of field strength and the dielectric function imaginary part but inversely correlated with the metal size. Therefore, high field intensity, large imaginary parts, and small size are required for strong optical absorption. However, there is an intrinsic dilemma between absorption and the local field.[116] Typically, a small imaginary part can bring an intense field but minimize plasmon decay to form energetic hot carriers; meanwhile, nanoparticles with large size have a strong electromagnetic field, but most LSPR energy decays through photon radiation. Fortunately, absorption-local fields can be balanced through geometric construction (*e.g.*, protruding tips), coupling with high imaginary part metals (Pd, Pt), assembling interparticle hotspots, and tuning the particle size.

Except the LSPR properties, the critical role of catalytic electronic states has been gradually unraveled, which largely determines the adsorption/desorption of molecules on the catalyst surface.[87,117] Considering that the surface plasmon energy distribution is non-homogeneous, local fields or hot carriers can greatly influence interfacial states, such as molecular polarities, electronic states, adsorption, *etc.*, in the regions with significant LSPR features. However, over the sites with poor plasmon energy, there are some blank spots where LSPR does not effectively affect the sites, and a thermal-driven process may not be negligible. Therefore, from the perspective of obtaining higher catalytic efficiency, optimizing the intrinsic ground electronic states may be one of the vital strategies. In addition to Fermi level engineering and metallic alloying we mentioned above, there exist some other approaches such as geometry or faceting control of activity metals, and intermetallic tuning (*i.e.*, ligand, ensemble, and strain effect) which have been successfully established for modifying electronic states. For example, it has been demonstrated that Pd–Au interface sites exhibit high activity and selectivity for FA decomposition by optimization of the arrangement of Pd and Au atoms through an ensemble

effect.[118] The Pd–PdO interface could decompose FA at a high rate with overcoming CO toxicity due to a special electronic state.[119] Therefore, to further improve catalytic performances, much attention should be paid to rationally designing efficient catalysts by considering both solar energy utilization and intrinsic electronic properties.

In addition, cheaper and more abundant Cu and Al elements can be developed as substitutes for precious metals, but the potential effects of easily oxidized surfaces on optical properties and catalytic rates must be recognized.

(3) Integrating local heat. The local surface plasmon decays in a non-radiative way, finally causing local heat. For FA dehydrogenation, a thermodynamically favorable process, heating should facilitate a higher yield. Most reported plasmon-involved systems apply a water bath to eliminate the heating effect induced by irradiation. From the point of view of energy utilization efficiency, this is wasteful because most energy is lost through heat transfer. However, attention should be paid to the quantitative distinction between thermal and non-thermal effects. Although the decoupling of these effects is greatly limited by the extended timescales and highly confined space, some studies and reviews have focused on this key question.[59,97,120,121] The contribution of hot carriers, local field, and local heat was distinguished through accurate temperature detection, optimized catalytic system design, or the application of *in situ* spectroscopy. In addition, excessive heating may also lead to poor product selectivity, generating carbon monoxide during HCOOH decomposition.[11,14,122,123] Therefore, the local thermal effect induced by LSPR is a double-edged sword. How to well balance photothermal and selectivity is one of the critical issues that must be addressed to make full use of plasmon energy.

With increasing attention and ongoing efforts on plasmonic catalysis, we look forward to more exciting discoveries, such as further improvements in selectivity/activity in this area, and predict that plasmonic catalysts probably will become the next generation of photocatalysts.

Conflicts of interest

There are no conflicts to declare.

Acknowledgements

Notes and references

1 H. Hou, X. Zeng and X. Zhang, *Angew. Chem., Int. Ed.*, 2020, **59**, 17356–17376.

2 Y. Li, X. Wei, L. Chen and J. Shi, *Angew. Chem., Int. Ed.*, 2021, **60**, 19550–19571.

3   H. Song, S. Luo, H. Huang, B. Deng and J. Ye, *ACS Energy Lett.*, 2022, **7**, 1043–1065.

4   S. Niaz, T. Manzoor and A. H. Pandith, *Renewable Sustainable Energy Rev.*, 2015, **50**, 457–469.

5   F. Valentini, V. Kozell, C. Petrucci, A. Marrocchi, Y. Gu, D. Gelman and L. Vaccaro, *Energy Environ. Sci.*, 2019, **12**, 2646–2664.

6   Z. Li and Q. Xu, *Acc. Chem. Res.*, 2017, **50**, 1449–1458.

7   K. Tedsree, T. Li, S. Jones, C. W. A. Chan, K. M. K. Yu, P. A. J. Bagot, E. A. Marquis, G. D. W. Smith and S. C. E. Tsang, *Nat. Nanotechnol.*, 2011, **6**, 302–307.

8   A. Gemenetzi, Y. Deligiannakis and M. Louloudi, *ACS Catal.*, 2023, **13**, 9905–9917.

9   X. Liu, D. Wang and Y. Li, *Nano Today*, 2012, **7**, 448–466.

10   M. Karatok, K. Duanmu, C. R. O'Connor, J. A. Boscoboinik, P. Sautet, R. J. Madix and C. M. Friend, *Chem. Sci.*, 2020, **11**, 6492–6499.

11   J. Zhu, J. Huang, J. Dai, R. Chen, X. Fu, Z. Wang, H. Liu and G. Li, *ACS Appl. Energy Mater.*, 2022, **5**, 10013–10022.

12   J. Zhu, J. Huang, J. Dai, L. Jiang, Y. Xu, R. Chen, L. Li, X. Fu, Z. Wang, H. Liu and G. Li, *ChemSusChem*, 2023, **16**, e202202069.

13   P. Liu, X. Gu, H. Zhang, J. Cheng, J. Song and H. Su, *Appl. Catal., B*, 2017, **204**, 497–504.

14   F. Tong, Z. Lou, X. Liang, F. Ma, W. Chen, Z. Wang, Y. Liu, P. Wang, H. Cheng, Y. Dai, Z. Zheng and B. Huang, *Appl. Catal., B*, 2020, **277**, 119226.

15   S. B. Zhang, M. Li, J. K. Zhao, H. Wang, X. L. Zhu, J. Y. Han and X. Liu, *Appl. Catal., B*, 2019, **252**, 24–32.

16   Z. Zheng, T. Tachikawa and T. Majima, *J. Am. Chem. Soc.*, 2015, **137**, 948–957.

17   Y. Zhang, S. He, W. Guo, Y. Hu, J. Huang, J. R. Mulcahy and W. D. Wei, *Chem. Rev.*, 2018, **118**, 2927–2954.

18   G. V. Hartland, *Chem. Rev.*, 2011, **111**, 3858–3887.

19   C. Brissaud, L. V. Besteiro, J. Y. Piquemal and M. Comesana-Hermo, *Sol. RRL*, 2023, **7**, 2300195.

20   M. L. Brongersma, N. J. Halas and P. Nordlander, *Nat. Nanotechnol.*, 2015, **10**, 25–34.

21   S. Linic, P. Christopher, H. Xin and A. Marimuthu, *Acc. Chem. Res.*, 2013, **46**, 1890–1899.

22   S. Linic, P. Christopher and D. B. Ingram, *Nat. Mater.*, 2011, **10**, 911–921.

23   M. W. Knight, N. S. King, L. Liu, H. O. Everitt, P. Nordlander and N. J. Halas, *ACS Nano*, 2014, **8**, 834–840.

24   H. Jing and H. Wang, *Chem. Mater.*, 2015, **27**, 2172–2180.

25   H. Jing, Q. Zhang, N. Large, C. Yu, D. A. Blom, P. Nordlander and H. Wang, *Nano Lett.*, 2014, **14**, 3674–3682.

26   Y. Xin, K. Yu, L. Zhang, Y. Yang, H. Yuan, H. Li, L. Wang and J. Zeng, *Adv. Mater.*, 2021, **33**, 2008145.

27   X. Sun, J. Yang, L. Sun, G. Yang, C. Liu, Y. Tao, Q. Cheng, C. Wang, H. Xu and Q. Zhang, *ACS Nano*, 2022, **16**, 19174–19186.

28   M. Ivanchenko and H. Jing, *Chem. Mater.*, 2023, **35**, 4598–4620.

29   J. Gargiulo, M. Herran, I. L. Violi, A. Sousa-Castillo, L. P. Martinez, S. Ezendam, M. Barella, H. Giesler, R. Grzeschik, S. Schluecker, S. A. Maier, F. D. Stefani and E. Cortes, *Nat. Commun.*, 2023, **14**, 3813.

30   H. Cheng, K. Fuku, Y. Kuwahara, K. Mori and H. Yamashita, *J. Mater. Chem. A*, 2015, **3**, 5244–5258.

31   P. Zhang, T. Wang and J. Gong, *Adv. Mater.*, 2015, **27**, 5328–5342.

32   M. Wang, M. Ye, J. Iocozzia, C. Lin and Z. Lin, *Adv. Sci.*, 2016, **3**, 1600024.

33   J. H. Park, Y. W. Cho and T. H. Kim, *Biosens.*, 2022, **12**, 180.

34   M. Fang, X. Tan, Z. Liu, B. Hu and X. Wang, *Research*, 2021, **2021**, 9794329.

35   M. Sun, Z. Wang and H. Wang, *Chem. Mater.*, 2022, **34**, 1965–1975.

36   G. G. Li, M. Sun, E. Villarreal, S. Pandey, S. R. Phillpot and H. Wang, *Langmuir*, 2018, **34**, 4340–4350.

37   Q. Zhang, L. Han, H. Jing, D. A. Blom, Y. Lin, H. L. Xing and H. Wang, *ACS Nano*, 2016, **10**, 2960–2974.

38   M. Herran, A. Sousa Castillo, C. Fan, S. Lee, W. Xie, M. Doeblinger, B. Auguie and E. Cortes, *Adv. Funct. Mater.*, 2022, **32**, 2203418.

39   M. Wen, K. Mori, Y. Kuwahara and H. Yamashita, *ACS Energy Lett.*, 2017, **2**, 1–7.

40   H. Liu, X. Y. Liu, W. W. Yang, M. Q. Shen, S. Geng, C. Yu, B. Shen and Y. S. Yu, *J. Mater. Chem. A*, 2019, **7**, 2022–2026.

41   L. P. Xiao, Y. S. Jun, B. H. Wu, D. Y. Liu, T. T. Chuong, F. A. Jie and G. D. Stucky, *J. Mater. Chem. A*, 2017, **5**, 6382–6387.

42   W. Hou and S. B. Cronin, *Adv. Funct. Mater.*, 2013, **23**, 1612–1619.

43   Z. Yin, Y. Wang, C. Song, L. Zheng, N. Ma, X. Liu, S. Li, L. Lin, M. Li, Y. Xu, W. Li, G. Hu, Z. Fang and D. Ma, *J. Am. Chem. Soc.*, 2018, **140**, 864–867.

44   R. Liu, Z. K. Zhou, Y. C. Yu, T. Zhang, H. Wang, G. Liu, Y. Wei, H. Chen and X. H. Wang, *Phys. Rev. Lett.*, 2017, **118**, 237401.

45   H. Kang, J. T. Buchman, R. S. Rodriguez, H. L. Ring, J. He, K. C. Bantz and C. L. Haynes, *Chem. Rev.*, 2019, **119**, 664–699.

46   H. Chen, L. Shao, Q. Li and J. Wang, *Chem. Soc. Rev.*, 2013, **42**, 2679–2724.

47   Y. Chen, Z. Fan, Z. Zhang, W. Niu, C. Li, N. Yang, B. Chen and H. Zhang, *Chem. Rev.*, 2018, **118**, 6409–6455.

48   Y. Xia, K. D. Gilroy, H. C. Peng and X. Xia, *Angew. Chem., Int. Ed.*, 2017, **56**, 60–95.

49   P. Zhao, N. Li and D. Astruc, *Coord. Chem. Rev.*, 2013, **257**, 638–665.

50   M. Ivanchenko, A. L. Carroll, A. B. Brothers and H. Jing, *Nanoscale Adv.*, 2022, **5**, 88–95.

51   Q. Zhang, N. Large, P. Nordlander and H. Wang, *J. Phys. Chem. Lett.*, 2014, **5**, 370–374.

52   S. Kim, S. Lee and S. Yoon, *ACS Appl. Mater. Interfaces*, 2022, **14**, 4163–4169.

53   L. T. M. Huynh, S. Kim and S. Yoon, *ACS Photonics*, 2022, **9**, 3260–3267.

54   L. Wang, M. Hasanzadeh Kafshgari and M. Meunier, *Adv. Funct. Mater.*, 2020, **30**, 2005400.

55 K. M. Mayer and J. H. Hafner, *Chem. Rev.*, 2011, **111**, 3828–3857.

56 V. Amendola, R. Pilot, M. Frasconi, O. M. Marago and M. A. Iati, *J. Phys.: Condens. Matter*, 2017, **29**, 203002.

57 B. Seemala, A. J. Therrien, M. Lou, K. Li, J. P. Finzel, J. Qi, P. Nordlander and P. Christopher, *ACS Energy Lett.*, 2019, **4**, 1803–1809.

58 K. Li, N. J. Hogan, M. J. Kale, N. J. Halas, P. Nordlander and P. Christopher, *Nano Lett.*, 2017, **17**, 3710–3717.

59 R. C. Elias and S. Linic, *J. Am. Chem. Soc.*, 2022, **144**, 19990–19998.

60 X. Jiang, J. Huang, Z. Bi, W. Ni, G. Gurzadyan, Y. Zhu and Z. Zhang, *Adv. Mater.*, 2022, **34**, 2109330.

61 G. W. P. Adhyaksa, S. W. Baek, G. I. Lee, D. K. Lee, J. Y. Lee and J. K. Kang, *ChemSusChem*, 2014, **7**, 2461–2468.

62 S. M. Meyer, J. Pettine, D. J. Nesbitt and C. J. Murphy, *J. Phys. Chem. C*, 2021, **125**, 16268–16278.

63 H. Jing and H. Wang, *CrystEngComm*, 2014, **16**, 9469–9477.

64 Q. Zhang, Y. Zhou, E. Villarreal, Y. Lin, S. Zou and H. Wang, *Nano Lett.*, 2015, **15**, 4161–4169.

65 M. Chen, Z. Ye, L. Wei, J. Yuan and L. Xiao, *J. Am. Chem. Soc.*, 2022, **144**, 12842–12849.

66 S. Chavez, U. Aslam and S. Linic, *ACS Energy Lett.*, 2018, **3**, 1590–1596.

67 K. Jiang, K. Xu, S. Zou and W. B. Cai, *J. Am. Chem. Soc.*, 2014, **136**, 4861–4864.

68 X. Qin, H. Li, S. Xie, K. Li, T.-W. Jiang, X.-Y. Ma, K. Jiang, Q. Zhang, O. Terasaki, Z. Wu and W. B. Cai, *ACS Catal.*, 2020, **10**, 3921–3932.

69 Z. L. Wang, J. M. Yan, Y. Ping, H. L. Wang, W. T. Zheng and Q. Jiang, *Angew. Chem., Int. Ed.*, 2013, **52**, 4406–4409.

70 R. Arrigo, M. E. Schuster, Z. Xie, Y. Yi, G. Wowsnick, L. L. Sun, K. E. Hermann, M. Friedrich, P. Kast, M. Haevecker, A. Knop Gericke and R. Schloegl, *ACS Catal.*, 2015, **5**, 2740–2753.

71 A. L. Wang, H. Xu, J. X. Feng, L. X. Ding, Y. X. Tong and G. R. Li, *J. Am. Chem. Soc.*, 2013, **135**, 10703–10709.

72 H. Xin, A. Vojvodic, J. Voss, J. K. Norskov and F. Abild-Pedersen, *Phys. Rev. B*, 2014, **89**, 115114.

73 Y. Guo, R. Zhang, S. Zhang, Y. Zhao, Q. Yang, Z. Huang, B. Dong and C. Zhi, *Energy Environ. Sci.*, 2021, **14**, 3938–3944.

74 J. Li, H. M. Yin, X. B. Li, E. Okunishi, Y. L. Shen, J. He, Z. K. Tang, W. X. Wang, E. Yucelen, C. Li, Y. Gong, L. Gu, S. Miao, L.-M. Liu, J. Luo and Y. Ding, *Nat. Energy*, 2017, **2**, 17111.

75 Y. Wang, L. Cao, N. J. Libretto, X. Li, C. Li, Y. Wan, C. He, J. Lee, J. Gregg, H. Zong, D. Su, J. T. Miller, T. Mueller and C. Wang, *J. Am. Chem. Soc.*, 2019, **141**, 16635–16642.

76 Y. Feng, G. Wang, Y. Chang, Y. Cheng, B. Sun, L. Wang, C. Chen and H. Zhang, *Nano Lett.*, 2019, **19**, 4478–4489.

77 H. Huang, H. Jia, Z. Liu, P. Gao, J. Zhao, Z. Luo, J. Yang and J. Zeng, *Angew. Chem., Int. Ed.*, 2017, **56**, 3594–3598.

78 L. Y. Zhang, C. X. Guo, H. Cao, S. Wang, Y. Ouyang, B. Xu, P. Guo and C. M. Li, *Chem. Eng. J.*, 2022, **431**, 133237.

79 J. N. Zhu, X. Q. Zhu, F. F. Cheng, P. Li, F. Wang, Y. W. Xiao and W. W. Xiong, *Appl. Catal., B*, 2019, **256**, 117830.

80 G. Liao, Y. Gong, L. Zhang, H. Gao, G. J. Yang and B. Fang, *Energy Environ. Sci.*, 2019, **12**, 2080–2147.

81 W. J. Ong, L. L. Tan, Y. H. Ng, S. T. Yong and S. P. Chai, *Chem. Rev.*, 2016, **116**, 7159–7329.

82 B. Gholipour, A. Zonouzi, M. Shokouhimehr and S. Rostamnia, *Sci. Rep.*, 2022, **12**, 13583.

83 C. Xu, X. Wang and J. Zhu, *J. Phys. Chem. C*, 2008, **112**, 19841–19845.

84 E. Peiris, S. Sarina, E. R. Waclawik, G. A. Ayoko, P. Han, J. Jia and H. Y. Zhu, *Angew. Chem., Int. Ed.*, 2019, **58**, 12032–12036.

85 S. Sarina, S. Bai, Y. Huang, C. Chen, J. Jia, E. Jaatinen, G. A. Ayoko, Z. Bao and H. Zhu, *Green Chem.*, 2014, **16**, 331–341.

86 Y. Dong, C. Hu, H. Xiong, R. Long and Y. Xiong, *ACS Catal.*, 2023, **13**, 6730–6743.

87 W. Jiang, B. Q. L. Low, R. Long, J. Low, H. Loh, K. Y. Tang, C. H. T. Chai, H. Zhu, H. Zhu, Z. Li, X. J. Loh, Y. Xiong and E. Ye, *ACS Nano*, 2023, **17**, 4193–4229.

88 S. Linic, U. Aslam, C. Boerigter and M. Morabito, *Nat. Mater.*, 2015, **14**, 567–576.

89 S. Linic, S. Chavez and R. Elias, *Nat. Mater.*, 2021, **20**, 916–924.

90 S. A. Lee and S. Link, *Acc. Chem. Res.*, 2021, **54**, 1950–1960.

91 T. G. Habteyes, S. Dhuey, E. Wood, D. Gargas, S. Cabrini, P. J. Schuck, A. P. Alivisatos and S. R. Leone, *ACS Nano*, 2012, **6**, 5702–5709.

92 U. Aslam, S. Chavez and S. Linic, *Nat. Nanotechnol.*, 2017, **12**, 1000–1005.

93 F. Tong, X. Liang, F. Ma, X. Bao, Z. Wang, Y. Liu, P. Wang, H. Cheng, Y. Dai, B. Huang and Z. Zheng, *ACS Catal.*, 2021, **11**, 3801–3809.

94 P. Wang, S. N. Steinmann, G. Fu, C. Michel and P. Sautet, *ACS Catal.*, 2017, **7**, 1955–1959.

95 B. Wu, J. Lee, S. Mubeen, Y. S. Jun, G. D. Stucky and M. Moskovits, *Adv. Opt. Mater.*, 2016, **4**, 1041–1046.

96 Y. Zhang, L. Yan, M. Guan, D. Chen, Z. Xu, H. Guo, S. Hu, S. Zhang, X. Liu, Z. Guo, S. Li and S. Meng, *Adv. Sci.*, 2022, **9**, 2102978.

97 H. Robatjazi, H. Zhao, D. F. Swearer, N. J. Hogan, L. Zhou, A. Alabastri, M. J. McClain, P. Nordlander and N. J. Halas, *Nat. Commun.*, 2017, **8**, 27.

98 L. Zhou, J. M. P. Martirez, J. Finzel, C. Zhang, D. F. Swearer, S. Tian, H. Robatjazi, M. Lou, L. Dong, L. Henderson, P. Christopher, E. A. Carter, P. Nordlander and N. J. Halas, *Nat. Energy*, 2020, **5**, 61–70.

99 D. F. Swearer, H. Zhao, L. Zhou, C. Zhang, H. Robatjazi, J. M. P. Martirez, C. M. Krauter, S. Yazdi, M. J. McClain, E. Ringe, E. A. Carter, P. Nordlander and N. J. Halas, *Proc. Natl. Acad. Sci. U.S.A.*, 2016, **113**, 8916–8920.

100 Z. Zhu, R. Tang, C. Li, X. An and L. He, *Adv. Sci.*, 2023, 2302568, DOI: **10.1002/advs.202302568**.

101 R. Ninakanti, F. Dingenen, R. Borah, H. Peeters and S. W. Verbruggen, *Top. Curr. Chem.*, 2022, **380**, 40.

102 M. Vadai, D. K. Angell, F. Hayee, K. Sytwu and J. A. Dionne, *Nat. Commun.*, 2018, **9**, 4658.

103 K. Sytwu, M. Vadai, F. Hayee, D. K. Angell, A. Dai, J. Dixon and J. A. Dionne, *Science*, 2021, **371**, 280–283.

104 C. Hu, X. Chen, J. Jin, Y. Han, S. Chen, H. Ju, J. Cai, Y. Qiu, C. Gao, C. Wang, Z. Qi, R. Long, L. Song, Z. Liu and Y. Xiong, *J. Am. Chem. Soc.*, 2019, **141**, 7807–7814.

105 C. Hu, X. Chen, J. Low, Y. Yang, H. Li, D. Wu, S. Chen, J. Jin, H. Li, H. Ju, C. Wang, Z. Lu, R. Long, L. Song and Y. Xiong, *Nat. Commun.*, 2023, **14**, 221.

106 F. X. Tong, X. Z. Liang, M. Liu, Z. Y. Wang, Y. Y. Liu, P. Wang, H. F. Cheng, Y. Dai, Z. K. Zheng and B. B. Huang, *ACS Catal.*, 2022, **12**, 3558–3565.

107 E. Cortes, R. Grzeschik, S. A. Maier and S. Schluecker, *Nat. Rev. Chem*, 2022, **6**, 259–274.

108 L. Langelueddecke, P. Singh and V. Deckert, *Appl. Spectrosc.*, 2015, **69**, 1357–1371.

109 T. Touzalin, A. L. Dauphin, S. Joiret, I. T. Lucas and E. Maisonhaute, *Phys. Chem. Chem. Phys.*, 2016, **18**, 15510–15513.

110 C. Gao, W. Lin, J. Wang, R. Wang and J. Wang, *Plasmonics*, 2018, **13**, 1343–1358.

111 J. F. Li, Y. J. Zhang, S. Y. Ding, R. Panneerselvam and Z. Q. Tian, *Chem. Rev.*, 2017, **117**, 5002–5069.

112 A. B. Zrimsek, N. Chiang, M. Mattei, S. Zaleski, M. O. McAnally, C. T. Chapman, A. I. Henry, G. C. Schatz and R. P. Van Duyne, *Chem. Rev.*, 2017, **117**, 7583–7613.

113 S. Y. Ding, E. M. You, Z. Q. Tian and M. Moskovits, *Chem. Soc. Rev.*, 2017, **46**, 4042–4076.

114 I. D. Barcelos, A. R. Cadore, A. B. Alencar, F. C. B. Maia, E. Mania, R. F. Oliveira, C. C. B. Bufon, A. Malachias, R. O. Freitas, R. L. Moreira and H. Chacham, *ACS Photonics*, 2018, **5**, 1912–1918.

115 H. A. Bechtel, S. C. Johnson, O. Khatib, E. A. Muller and M. B. Raschke, *Surf. Sci. Rep.*, 2020, **75**, 100493.

116 P. Christopher and M. Moskovits, in *Annual Review of Physical Chemistry*, ed. M. A. Johnson and T. J. Martinez, 2017, vol. 68, pp. 379–398.

117 K. Sytwu, M. Vadai and J. A. Dionne, *Adv. Phys.: X*, 2019, **4**, 1619480.

118 W. Y. Yu, G. M. Mullen, D. W. Flaherty and C. B. Mullins, *J. Am. Chem. Soc.*, 2014, **136**, 11070–11078.

119 Q. Lv, Q. L. Meng, W. W. Liu, N. Sun, K. Jiang, L. P. Ma, Z. Q. Peng, W. B. Cai, C. P. Liu, J. J. Ge, L. M. Liu and W. Xing, *J. Phys. Chem. C*, 2018, **122**, 2081–2088.

120 K. Chen and H. Wang, *Nano Lett.*, 2023, **23**, 2870–2876.

121 Q. Zhang, Y. Zhou, X. Fu, E. Villarreal, L. Sun, S. Zou and H. Wang, *J. Phys. Chem. C*, 2019, **123**, 26695–26704.

122 J. Eppinger and K. W. Huang, *ACS Energy Lett.*, 2017, **2**, 188–195.

123 I. Dutta, S. Chatterjee, H. Cheng, R. K. Parsapur, Z. Liu, Z. Li, E. Ye, H. Kawanami, J. S. C. Low, Z. Lai, X. J. Loh and K. W. Huang, *Adv. Energy Mater.*, 2022, **12**, 2103799.